Research Square

Preprints are preliminary reports that have not undergone peer review.
They should not be considered conclusive, used to inform clinical practice,
or referenced by the media as validated information.

Finite element comparison of three rotator cuff repair configurations across shoulder abduction angles: a static biomechanical study

Weipeng Zheng
The Third Affiliated Hospital of Guangzhou University of Chinese Medicine
Qirun Liu
Guangzhou University of Chinese Medicine
Xingyi Li
Guangzhou University of Chinese Medicine
Yiqi Yang
The Third Affiliated Hospital of Guangzhou University of Chinese Medicine
Sheng Chen
The Third Affiliated Hospital of Guangzhou University of Chinese Medicine
Yuke Song
The Third Affiliated Hospital of Guangzhou University of Chinese Medicine
Zhihao Liao
The Third Affiliated Hospital of Guangzhou University of Chinese Medicine
Zhijun Liu
The Third Affiliated Hospital of Guangzhou University of Chinese Medicine
Hewei Wei
whwhou@163.com

The Third Affiliated Hospital of Guangzhou University of Chinese Medicine

Research Article

Keywords: rotator cuff repair, finite element analysis, suture configuration, double-locking-loop, shoulder abduction, biomechanics

Posted Date: November 10th, 2026

DOI: https://doi.org/10.21203/rs.3.rs-11421054/v1

License: This work is licensed under a Creative Commons Attribution 4.0 International License.
Read Full License

Additional Declarations: No competing interests reported.

Abstract

Background

Rotator cuff repair constructs may differ in the distribution of tendon and suture stresses under early postoperative loading. This finite element study compared three suture configurations across three modeled shoulder abduction angles.

Methods

A three-dimensional shoulder model was constructed using computed tomography data from one healthy male volunteer. Cross single-row, double-row, and double-locking-loop repair configurations were simulated at 0°, 45°, and 90° of abduction (nine deterministic models). The distal humerus was fixed and a 100 N static tensile load was applied to the free end of the supraspinatus tendon. Tendon, suture, cartilage, and humeral suture-tunnel stresses and construct displacements were evaluated.

Results

The double-locking-loop construct had the lowest modeled tendon and suture von Mises stresses and tendon displacements at all three angles. Its peak suture stresses were 1.2985, 1.6325, and 0.83125 MPa at 0°, 45°, and 90°, respectively: reductions of 54.4%–65.4% relative to cross single-row and 32.2%–51.4% relative to double-row repairs. Corresponding tendon displacements were 0.074922, 0.084226, and 0.054456 mm. Differences were descriptive outputs of deterministic simulations, not estimates of clinical efficacy.

Conclusions

Under the assumed geometry, linear-elastic material properties, bonded interfaces, and static loading, the double-locking-loop configuration yielded lower predicted local stresses and displacements than the other two configurations. These computational findings require verification and experimental validation and cannot establish improved tendon healing, reduced retears, or optimal rehabilitation positioning.

Background

Rotator cuff tears commonly involve the supraspinatus tendon and are associated with shoulder pain, weakness, and functional limitation [1, 2]. Despite advances in arthroscopic repair, structural failure remains a clinical concern [3–5]. Before biological tendon-to-bone healing is established, load transfer through the repair construct depends partly on its initial mechanical properties.

Suture arrangement affects where tensile loads are transmitted into tendon and bone. Single-row constructs use a limited number of fixation paths, whereas double-row constructs can improve footprint coverage; however, the local stress distribution depends on the specific geometry, penetration pattern, and tensioning [6–9]. Locking-loop designs represent another means of tendon capture, although their relative stress distributions under different modeled shoulder positions remain uncertain.

Finite element analysis can characterize modeled internal stresses and displacements that are difficult to observe directly in bench tests, but the results remain dependent on material, geometry, load, and interface assumptions [10–24]. We therefore compared cross single-row, double-row, and double-locking-loop repairs at 0°, 45°, and 90° of shoulder abduction. We hypothesized that the modeled double-locking-loop configuration would exhibit lower peak local stress and displacement under identical static loading.

Methods

Study design

A deterministic, static finite element comparison was performed using a single computed tomography-derived shoulder geometry. Three repair configurations were combined with three modeled abduction angles, producing nine configurations. The same nominal material properties, applied force, and distal fixation protocol were used for comparisons; no between-subject variability was simulated.

Imaging data, CT acquisition, and ethical approval

Computed tomography (CT) data were obtained from the right shoulder of one healthy male volunteer with no history of shoulder disease. Scanning was performed using an Aquilion CT system (Toshiba) with helical axial acquisition in a head-first supine position. The tube voltage was 120 kVp, tube current was 300 mA, exposure time was 750 ms, and tube-current–time product was 225 mAs. Axial images were reconstructed with a 2.0-mm slice thickness, a 237.5-mm reconstruction diameter, 0° gantry tilt, and an FC18 convolution kernel, and were exported in Digital Imaging and Communications in Medicine (DICOM) format. The study protocol was approved by the Guangzhou University of Chinese Medicine Third Affiliated Hospital Institutional Ethics Committee (approval no. KY [2019] 002), and written informed consent for participation and publication was obtained from the volunteer. The repair constructs were generated using healthy shoulder geometry; a patient-specific rotator cuff tear was not reconstructed.

Geometry reconstruction and model assembly

Computed tomography data were processed in Mimics 21.0 (Materialise, Leuven, Belgium). Threshold segmentation, region growing, manual slice editing, and mask filling were used to extract the humeral

geometry. The model was exported in stereolithography (STL) format and refined in Geomagic 2021 (3D Systems, Rock Hill, SC, USA) by denoising, smoothing, surface repair, and curve fitting. The geometry was then imported into SolidWorks 2025 (Dassault Systèmes, Vélizy-Villacoublay, France), where idealized cartilage, supraspinatus tendon, anchors, and sutures were assembled. Surface and interference checks were performed before finite element preprocessing (Fig. 1). Complete numerical specifications for the idealized tendon, anchor, and suture geometries were not documented, limiting exact reproduction of the modeled repair constructs.

Repair configurations and model groups

Three repair configurations were constructed: cross single-row, double-row, and double-locking-loop. Each configuration was evaluated at 0°, 45°, and 90° of shoulder abduction, yielding nine models. The same baseline geometry, material properties, 100 N load magnitude, and distal fixation were used for the corresponding comparisons.

Material properties

Cortical bone, cancellous bone, cartilage, supraspinatus tendon, anchors, and sutures were assigned homogeneous, isotropic, linear-elastic properties as a modeling simplification [10, 12, 13, 25–27]. These assumptions do not represent native tendon anisotropy, nonlinear recruitment, or time-dependent deformation. The assigned moduli and Poisson ratios are shown in Table 1.

Table 1
Material properties assigned to finite element models.

Material	Elastic modulus (MPa)	Poisson ratio
Cortical bone	13400	0.30
Cancellous bone	2000	0.26
Cartilage	400	0.40
Supraspinatus tendon	1200	0.40
Anchor	5500	0.40
Suture	591	0.45

Note: Elastic modulus is in MPa. All listed materials were modeled as homogeneous, isotropic, and linearly elastic.

Mesh generation

Models were imported into the Static Structural module of Ansys Workbench 23.0 (Ansys Inc., Canonsburg, PA, USA) and meshed with tetrahedral elements. Mesh quality was assessed using

orthogonal quality, Jacobian ratio, and skewness. The mesh-quality screening criteria were orthogonal quality > 0.25, Jacobian ratio > 0.5, and skewness < 0.8. Element and node counts are given in Table 2. A formal mesh-convergence study was not documented; therefore, the mesh independence of local peak-stress estimates could not be established.

Table 2
Mesh sizes across nine repair configurations.

Model	Elements	Nodes
0° cross single-row	492412	869530
0° double-row	492921	872373
0° double-locking-loop	543528	962209
45° cross single-row	493271	869552
45° double-row	491541	869417
45° double-locking-loop	688726	1207538
90° cross single-row	509652	898139
90° double-row	515212	909116
90° double-locking-loop	440873	784159
Note: These counts describe model discretization; they do not constitute a mesh-convergence assessment.		

Boundary, loading, and contact conditions

The distal humeral surface was fully fixed, and a 100 N tensile load was applied to the free end of the supraspinatus tendon in each simulation [19, 25] (Fig. 2). Anchor–bone, suture–anchor, suture–tendon, and bone–cartilage interfaces were modeled as bonded contacts. This assumption prevents relative sliding or separation and does not represent frictional slip, suture cut-through, or local detachment. The load-vector components and reference coordinate system for the three modeled abduction positions were not fully specified, limiting independent reproduction of the angle-specific boundary conditions.

Outcome measures and data analysis

Outcome measures and data analysis
Reported outcomes included peak von Mises and maximum principal stresses in the supraspinatus tendon; peak von Mises stresses in sutures, cartilage, and the humeral suture-tunnel region; and maximum tendon and suture displacements. Because the analysis comprised nine deterministic

calculations using one geometry, outcomes are descriptive; conventional inferential statistics, participant-level variance, and P values are not applicable.

Use of AI-assisted tools in manuscript preparation

ChatGPT (OpenAI) was used to assist with English-language editing, formatting, and consistency review. It was not used to generate finite element data or execute simulations. The authors retain responsibility for verifying the scientific content and approving the final submitted version.

Results

Overall findings

All nine static model solutions were obtained. Computed stress concentrations appeared near tendon penetration sites, suture turns or crossings, cartilage margins, and the humeral suture-tunnel region. The largest modeled displacements generally occurred near the free tendon end or along loaded suture segments. Stress results are summarized in Tables 3 and 4, and displacement results are shown in Table 5. Figures 1 and 2 depict the model configurations and boundary conditions; Figs. 3–5 summarize peak stress values and modeled displacements.

Tendon and suture stress

At 0°, 45°, and 90°, peak tendon von Mises stresses in the double-locking-loop configuration were 2.3763, 2.4762, and 1.8939 MPa, respectively. Relative to cross single-row repairs, these represent reductions of 6.2%, 26.5%, and 37.2%; relative to double-row repairs, reductions were 39.7%, 42.4%, and 27.5%. Peak suture von Mises stresses were 1.2985, 1.6325, and 0.83125 MPa, corresponding to reductions of 63.6%, 54.4%, and 65.4% compared with cross single-row and 49.1%, 51.4%, and 32.2% compared with double-row configurations, respectively (Table 3).

Table 3
Computed tendon and suture stresses.

Abduction angle	Repair configuration	Tendon von Mises stress (MPa)	Tendon maximum principal stress (MPa)	Suture von Mises stress (MPa)
0°	Cross single-row	2.5344	2.7531	3.5687
0°	Double-row	3.9439	4.0719	2.5502
0°	Double-locking-loop	2.3763	2.5547	1.2985
45°	Cross single-row	3.3702	3.3792	3.5803
45°	Double-row	4.2974	4.4643	3.3590
45°	Double-locking-loop	2.4762	2.7873	1.6325
90°	Cross single-row	3.0144	3.0519	2.4050
90°	Double-row	2.6114	2.5908	1.2260
90°	Double-locking-loop	1.8939	2.2773	0.83125

Note: These are deterministic peak numerical outputs, not experimental measurements.

Displacement and bone-cartilage stress

Modeled tendon displacements in the double-locking-loop configuration were 0.074922, 0.084226, and 0.054456 mm at 0°, 45°, and 90°, respectively, and were the lowest of the three configurations at each angle. Suture displacements showed the same ranking at each angle (Table 5). Cartilage and humeral suture-tunnel von Mises stresses were also numerically lower in the double-locking-loop configuration than in both comparators at each of the three modeled angles (Table 4).

Table 4
Computed cartilage and humeral suture-tunnel stresses.

Abduction angle	Repair configuration	Cartilage von Mises stress (MPa)	Humeral suture-tunnel von Mises stress (MPa)
0°	Cross single-row	1.6365	9.1034
0°	Double-row	1.6662	2.1960
0°	Double-locking-loop	1.3349	1.9492
45°	Cross single-row	1.2412	3.1357
45°	Double-row	1.2790	1.7194
45°	Double-locking-loop	0.98691	1.6364
90°	Cross single-row	0.31228	1.6842
90°	Double-row	0.31697	1.0315
90°	Double-locking-loop	0.18753	0.91425

Note: Peak von Mises stresses are reported for model-defined regions.

Table 5
Computed tendon and suture displacements.

Abduction angle	Repair configuration	Tendon displacement (mm)	Suture displacement (mm)
0°	Cross single-row	0.12961	0.054522
0°	Double-row	0.13069	0.057111
0°	Double-locking-loop	0.074922	0.052432
45°	Cross single-row	0.17403	0.046839
45°	Double-row	0.17530	0.049553
45°	Double-locking-loop	0.084226	0.029729
90°	Cross single-row	0.062999	0.028955
90°	Double-row	0.063636	0.025280
90°	Double-locking-loop	0.054456	0.019638

Note: Values represent the maximum model-predicted displacements under 100 N static loading.

Discussion

Principal findings

Under the specified static loading and interface assumptions, the double-locking-loop configuration generated the lowest peak tendon and suture von Mises stresses and tendon and suture displacements among the three modeled repairs across all abduction angles. The comparative ranking was consistent, although the magnitude of the differences varied by endpoint and position. The results are model-based stress and displacement predictions, not evidence of greater failure load, improved tendon-to-bone healing, or superior clinical outcomes.

Possible biomechanical explanation

One possible explanation for the computed differences is the geometry of the modeled suture path and the resulting distribution of traction among tendon regions. However, all suture-tendon contacts were fully bonded. As a consequence, the present analysis cannot directly test frictional grip, suture migration, cutting through the tendon, or failure at the repair interface. Any proposed mechanism involving resistance to slippage or cut-through remains speculative and requires contact-sensitive modeling and experimental testing [14–16, 22, 24].

Effect of shoulder abduction

Changing the modeled abduction angle altered the computed response, likely through changes in relative geometry and the direction of load transfer, as in prior computational analyses of shoulder loading [17–20]. The difference in tendon displacement between the configurations was most pronounced at 45° for the modeled conditions. This should not be construed as a recommendation for postoperative arm positioning: the model did not incorporate scapulothoracic motion, active muscle forces, rehabilitation loading, or anatomic variation.

Clinical relevance

Finite element comparisons can help prioritize hypotheses for bench testing and identify local regions deserving closer experimental attention. They do not, by themselves, demonstrate lower retear risk or justify a change in surgical technique or rehabilitation protocol. Native tissue quality, tear pattern, anchor fixation, suture tensioning, cyclic loading, joint kinematics, and biological healing can materially affect clinical performance [1–9, 28–30].

Limitations

Several limitations affect interpretation. The geometry was derived from one healthy volunteer, and tendon and cartilage shapes were idealized rather than reconstructed from subject-specific magnetic resonance imaging. Material behavior was homogeneous, isotropic, and linear elastic, and all modeled interfaces were bonded; friction, slip, separation, tendon damage, and cyclic fatigue were therefore excluded. Loading was limited to one 100 N static condition. No results from formal mesh-convergence testing, parameter-sensitivity analysis, or independent experimental validation were documented. Incomplete specification of repair geometry and angle-specific loading vectors further limits exact

reproduction of the simulations. Peak stress magnitudes, especially local maxima near contacts and penetrations, may be sensitive to mesh density and interface assumptions. The findings should therefore be interpreted as a hypothesis-generating computational comparison rather than a validated prediction of clinical performance.

Conclusions

Under the assumptions used in these deterministic static simulations, the double-locking-loop configuration showed lower predicted peak tendon and suture stresses and lower modeled tendon and suture displacements than the cross single-row and double-row configurations at each modeled abduction angle. The magnitude of the differences varied by outcome and angle. These results are conditional on a single CT-derived geometry, simplified linear-elastic material properties, bonded interfaces, and a 100 N static load. They do not establish improved tendon-to-bone healing, reduced retear risk, greater failure resistance, or a preferred postoperative shoulder position. Mesh-convergence testing, sensitivity analysis, and independent mechanical validation are needed before clinical implications can be considered.

Abbreviations

CAD
computer-aided design
CT
computed tomography
DICOM
Digital Imaging and Communications in Medicine.

Declarations

Ethics approval and consent to participate

The study protocol was approved by the Guangzhou University of Chinese Medicine Third Affiliated Hospital Institutional Ethics Committee (approval no. KY [2019] 002). Written informed consent for participation was obtained from the volunteer.

Clinical trial number

not applicable.

Consent for publication

Written informed consent for publication was obtained from the volunteer.

Availability of data and materials

The numerical outputs supporting this computational comparison are provided in Tables 1–5 and in the machine-readable dataset [see Additional file 1]. The original CT DICOM images are not publicly available because they constitute individual-level human imaging data subject to privacy and institutional access restrictions. The native ANSYS and computer-aided design (CAD) model project files are no longer available to the authors. Consequently, the numerical dataset enables reanalysis of reported outcomes but not independent recreation of the finite element simulation. Access to identifiable imaging data would require institutional authorization.

Competing interests

The authors declare that they have no competing interests.

Funding

This work was supported by the Scientific Research Open Foundation of Guangdong Institute of Traditional Chinese Medicine Bone Trauma (No. GYH202201-02).

Authors' contributions

WZ (Weipeng Zheng): Conceptualization, Methodology, Investigation, Formal analysis, Visualization, Writing – original draft. QL (Qirun Liu): Methodology, Software, Data curation, Formal analysis, Validation, Visualization, Writing – original draft. XL (Xingyi Li): Methodology, Software, Investigation, Data curation, Validation, Writing – original draft. YY (Yiqi Yang): Investigation, Data curation, Validation. SC (Sheng Chen): Methodology, Resources, Validation, Writing – review & editing. YS (Yuke Song): Formal analysis, Visualization, Data curation, Writing – review & editing. ZHL (Zhihao Liao): Software, Investigation, Validation, Visualization. ZJL (Zhijun Liu): Supervision, Resources, Project administration, Writing – review & editing. HW (Hewei Wei): Conceptualization, Supervision, Funding acquisition, Project administration, Resources, Writing – review & editing. Weipeng Zheng, Qirun Liu, and Xingyi Li contributed equally to this work and share first authorship. All authors reviewed and approved the final manuscript.

Acknowledgements

The authors would like to thank all members of the research team for their valuable assistance and support throughout this study.

References

1. Bedi A, Bishop J, Keener J, et al. Rotator cuff tears. Nat Rev Dis Primers. 2024;10(1):8.
2. Moran TE, Werner BC. Surgery and rotator cuff disease: a review of the natural history, indications, and outcomes of nonoperative and operative treatment of rotator cuff tears. Clin Sports Med. 2023;42(1):1–24.
3. Mandaleson A. Re-tears after rotator cuff repair: current concepts review. J Clin Orthop Trauma. 2021;19:168–74.
4. Lee YS, Jeong JY, Park CD, et al. Evaluation of the risk factors for a rotator cuff retear after repair surgery. Am J Sports Med. 2017;45(8):1755–61.
5. Zhao J, Luo M, Pan J, et al. Risk factors affecting rotator cuff retear after arthroscopic repair: a meta-analysis and systematic review. J Shoulder Elb Surg. 2021;30(11):2660–70.
6. Lee TQ. Current biomechanical concepts for rotator cuff repair. Clin Orthop Surg. 2013;5(2):89–97.
7. Rossi LA, Rodeo SA, Chahla J, et al. Current concepts in rotator cuff repair techniques: biomechanical, functional, and structural outcomes. Orthop J Sports Med. 2019;7(9):2325967119868674.
8. Gu Z, Wu S, Yang Y, et al. Comparison of arthroscopic single-row and double-row repair for rotator cuff injuries with different tear sizes: a systematic review and meta-analysis. Orthop J Sports Med. 2023;11(8):23259671231180854.
9. Khazzam M, Sager B, Box HN, et al. The effect of age on risk of retear after rotator cuff repair: a systematic review and meta-analysis. JSES Int. 2020;4(3):625–31.
10. Erdemir A, Guess TM, Halloran J, et al. Considerations for reporting finite element analysis studies in biomechanics. J Biomech. 2012;45(4):625–33.
11. Oefner C, Herrmann S, Kebbach M, et al. Reporting checklist for verification and validation of finite element analysis in orthopedic and trauma biomechanics. Med Eng Phys. 2021;92:25–32.
12. Ji K, Yu H, Chen G, Pan J, Li J. Finite element analysis of arthroscopic repair of rotator cuff injury with different transosseous techniques. Zhongguo Gu Shang. 2022;35:990–5. (in Chinese).
13. Mantovani M, Pellegrini A, Garofalo P, et al. A 3D finite element model for geometrical and mechanical comparison of different supraspinatus repair techniques. J Shoulder Elb Surg. 2016;25(4):557–63.
14. Funakoshi T, Suenaga N, Sano H, et al. In vitro and finite element analysis of a novel rotator cuff fixation technique. J Shoulder Elb Surg. 2008;17(6):986–92.
15. Sano H, Yamashita T, Wakabayashi I, et al. Stress distribution in the supraspinatus tendon after tendon repair: suture anchors versus transosseous suture fixation. Am J Sports Med. 2007;35(4):542–6.

16. Sano H, Komatsuda T, Inawashiro T, et al. Comparison between single and double suture passing techniques in the suture bridge rotator cuff repair with a 2-mm tape: a simulation study using a three-dimensional finite element method. J Orthop Sci. 2021;26(2):207–12.
17. Garcia M, Hedayatzadeh Razavi A, Caro D, et al. Finite element-based evaluation of the supraspinatus tendon biomechanical environment necessitates better clinical management based on tear location and thickness. Sci Rep. 2024;14(1):26323.
18. Yang Z, Xu G, Yang J, et al. Finite element study of the biomechanical effects on the rotator cuff under load. Front Bioeng Biotechnol. 2023;11:1193376.
19. Yang Z, Xu G, Yang J, et al. Effect of different loads on the shoulder in abduction postures: a finite element analysis. Sci Rep. 2023;13(1):9490.
20. Wang H, Chen L, Xu G, et al. Biomechanical effects of deltoid muscle atrophy on rotator cuff tissue: a finite element study. Sci Rep. 2024;14(1):17592.
21. Williamson P, Garcia M, Momenzadeh K, et al. A validated three-dimensional, heterogenous finite element model of the rotator cuff and the effects of collagen orientation. Ann Biomed Eng. 2023;51(5):1002–13.
22. Quental C, Reis J, Folgado J, et al. Comparison of 3 supraspinatus tendon repair techniques - a 3D computational finite element analysis. Comput Methods Biomech Biomed Engin. 2020;23(16):1387–94.
23. Redepenning DH, Ludewig PM, Looft JM. Finite element analysis of the rotator cuff: a systematic review. Clin Biomech (Bristol). 2020;71:73–85.
24. Zhong Y, Yu C, Feng S, et al. Optimal suturing techniques in patch-bridging reconstruction for massive rotator cuff tears: a finite element analysis. Asia Pac J Sports Med Arthrosc Rehabil Technol. 2025;39:22–9.
25. Baohu R, Qi Y, Tao L, Wang Y, Wei B, Li X, et al. A finite element analysis of the insertion angle of the metal anchor screw for rotator cuff injury repair. Chin J Shoulder Elb Surg (Electronic Edition). 2019;7:56–62. (in Chinese).
26. Wakabayashi I, Itoi E, Sano H, et al. Mechanical environment of the supraspinatus tendon: a two-dimensional finite element model analysis. J Shoulder Elb Surg. 2003;12(6):612–7.
27. Luo ZP, Hsu HC, Grabowski JJ, et al. Mechanical environment associated with rotator cuff tears. J Shoulder Elb Surg. 1998;7(6):616–20.
28. Dey Hazra ME, Dey Hazra RO, Hanson JA, et al. Treatment options for massive irreparable rotator cuff tears: a review of arthroscopic surgical options. EFORT Open Rev. 2023;8(1):35–44.
29. Darbandi AD, Cohn M, Credille K, et al. A systematic review and meta-analysis of risk factors for the increased incidence of revision surgery after arthroscopic rotator cuff repair. Am J Sports Med. 2024;52(5):1374–83.
30. Baur A, Lemons W, Protzuk O, et al. Early rotator cuff repair yields lower retear rates and superior functional outcomes: a systematic review and meta-analysis. J Clin Med. 2025;14(15):5552.

Figures

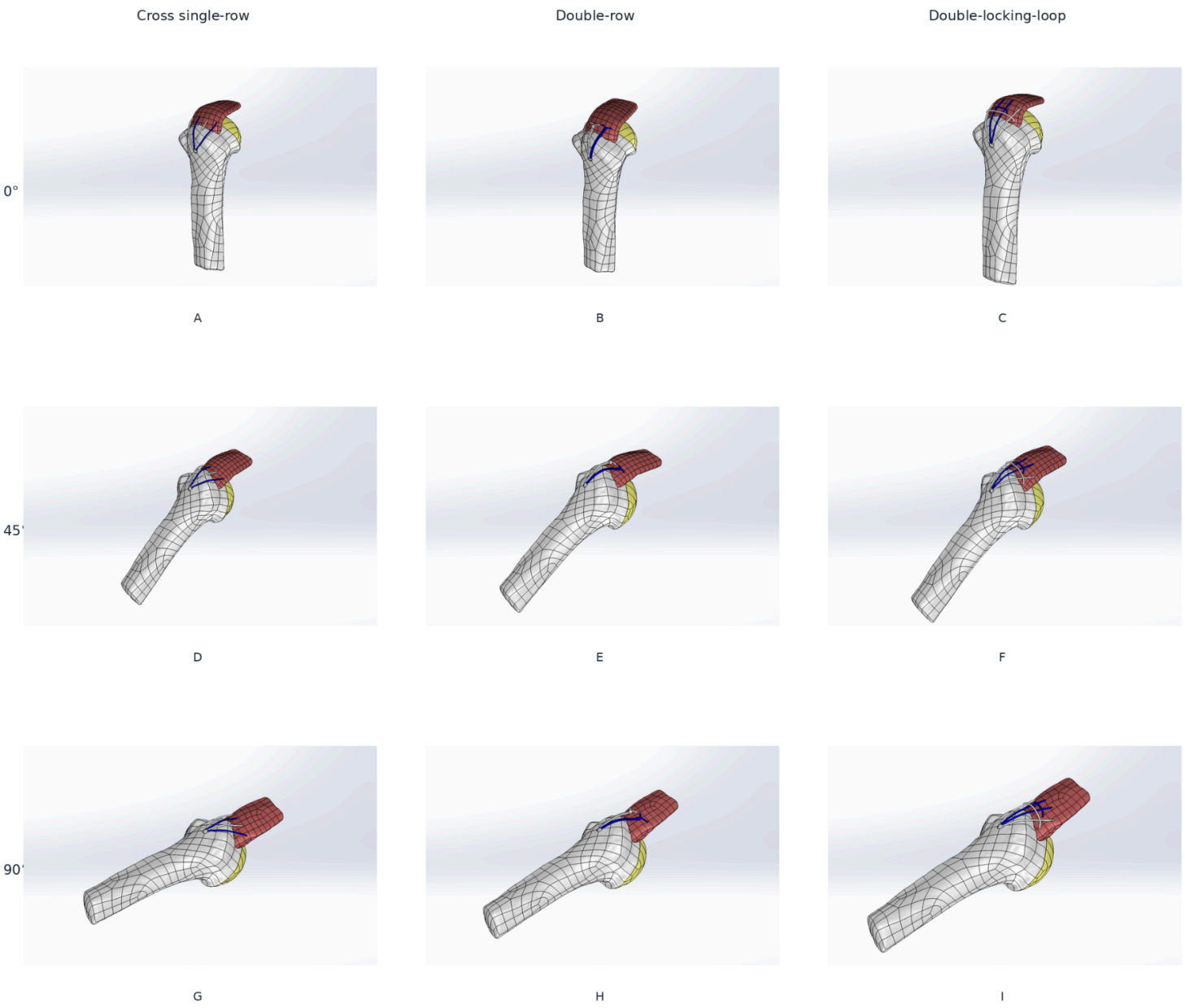


Figure 1

Nine finite element repair models. The 3 × 3 arrangement shows shoulder abduction angles of 0°, 45°, and 90° (rows) and the cross single-row, double-row, and double-locking-loop configurations (columns). Panels are composites of archived simulation images showing the corresponding analyzed configurations.

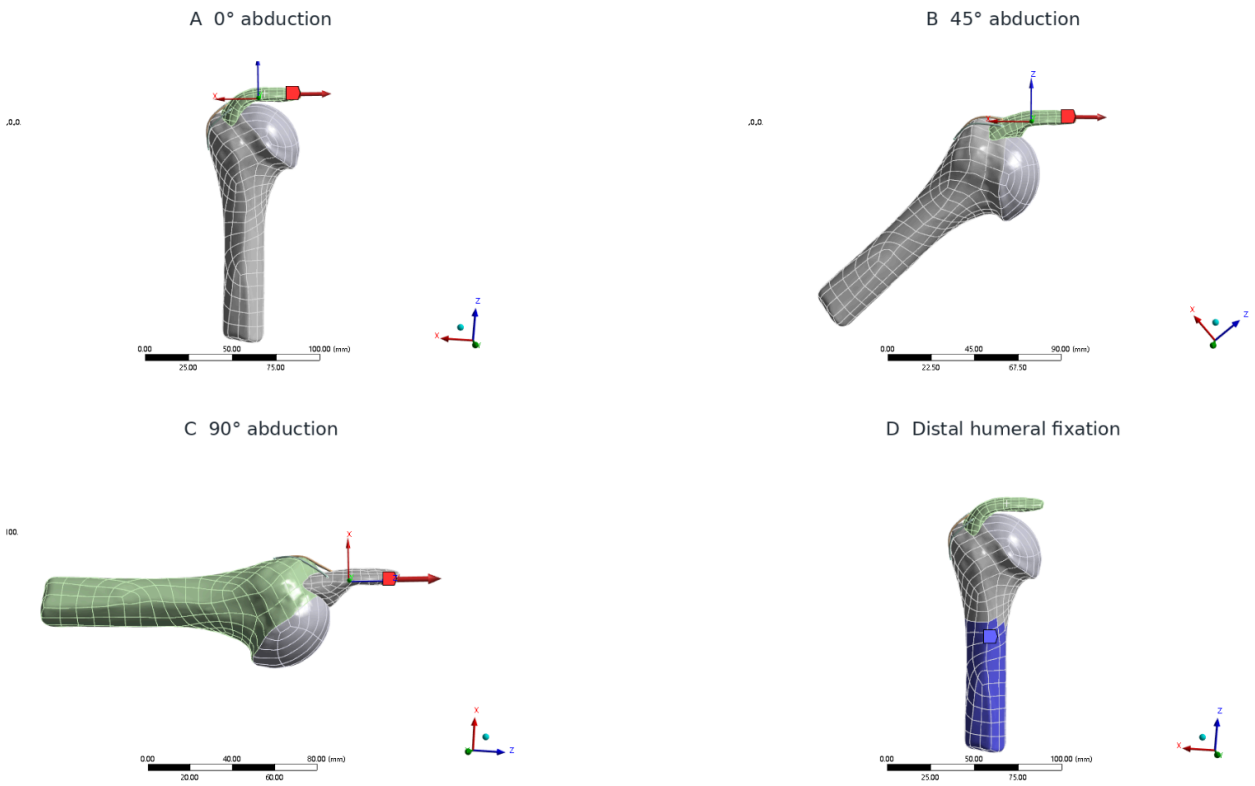


Figure 2

Modeled loading directions at three abduction angles. Panels A–C show the 100 N tensile load applied at the free end of the supraspinatus tendon in the models at 0°, 45°, and 90° of abduction, respectively. Panel D shows the fully constrained distal humeral region. Images are taken from the original finite element simulation outputs.

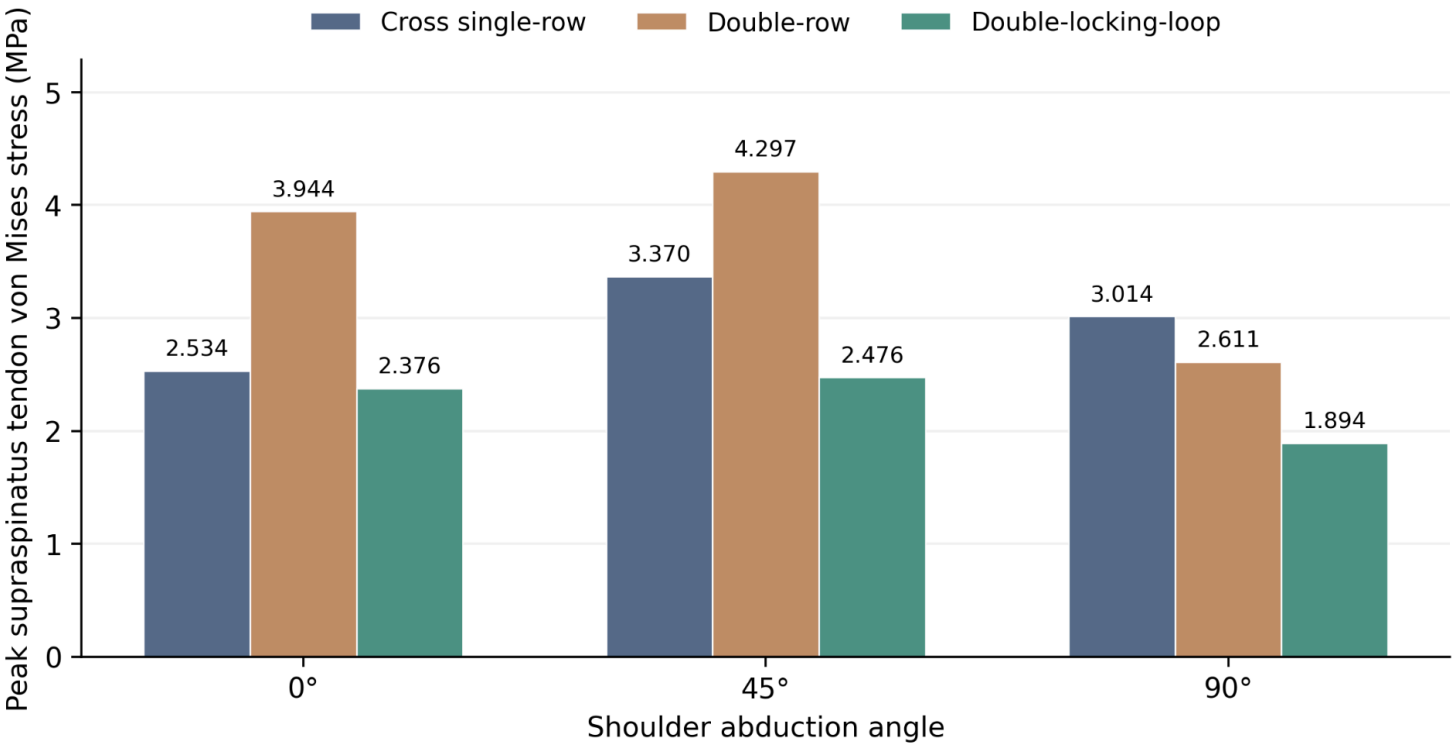


Figure 3

Peak supraspinatus tendon von Mises stress. Peak tendon von Mises stresses (MPa) from the nine deterministic finite element models, plotted by abduction angle and repair configuration. Bars represent single computational outcomes and are not estimates of biological variability; no error bars or inferential tests are shown.

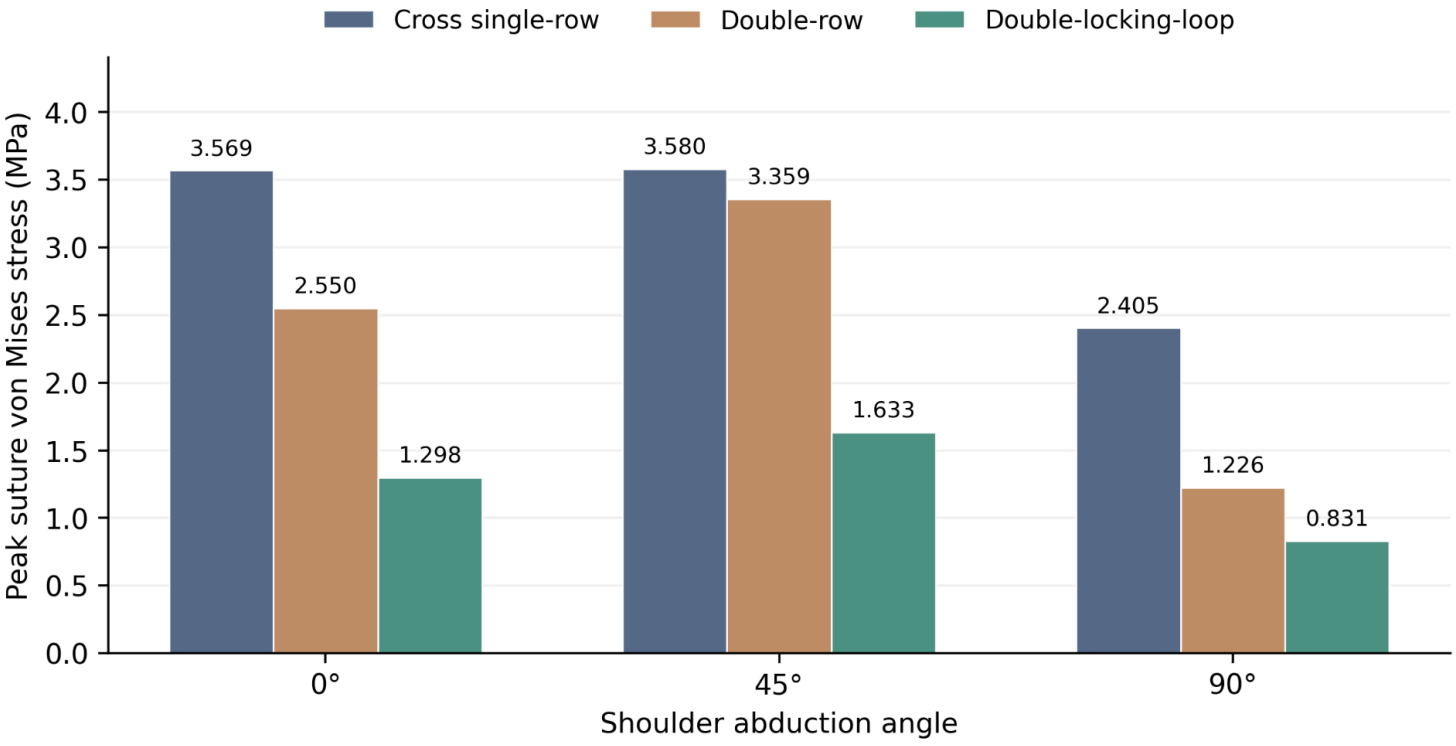


Figure 4

Peak suture von Mises stress. Peak suture von Mises stresses (MPa) for cross single-row, double-row, and double-locking-loop repairs at the three modeled abduction angles. Bars represent deterministic simulation outputs, not replicate measurements.

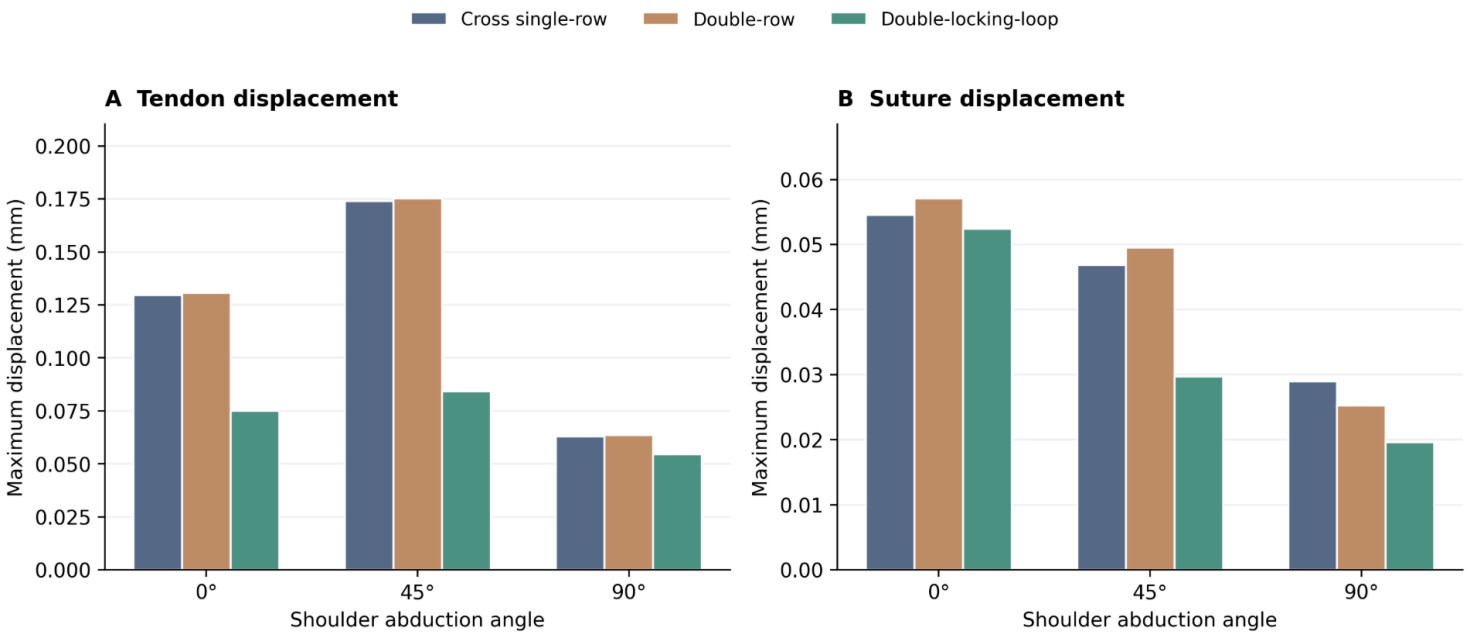


Figure 5

Modeled tendon and suture displacements. Maximum predicted displacements (mm) of the supraspinatus tendon (A) and the suture system (B) under 100 N static loading. Values are descriptive outputs from the nine deterministic models, without repeated specimens or uncertainty intervals.

Supplementary Files

This is a list of supplementary files associated with this preprint. Click to download.

- Additionalfile.csv